On the Development of a Second-Order Bistatic Radar Cross Section of the Ocean Surface: A High-Frequency Result for a Finite Scattering Patch

Eric Gill, *Senior Member, IEEE*, Weimin Huang, and John Walsh

***Abstract*—The development of a model for the second-order bistatic high-frequency (HF) radar cross section on an ocean surface patch remote from the transmitter and receiver is addressed. A new approach is taken that allows a direct comparison with existing monostatic cross sections for finite regions of the ocean surface. The derivation starts with a general expression for the bistatically received second-order electric field in which the scattering surface is assumed to be of small height and slope. The source field is taken to be that of a vertically polarized dipole, and it is assumed that the ocean surface can be described, as is usually done, by a Fourier series in which the coefficients are zero-mean Gaussian random variables. Subsequently, a bistatic cross section of the surface, normalized to patch area, is derived. The result is verified by the following two means: 1) the complete form of the bistatic HF radar cross section in backscattering case is shown to contain an earlier monostatic result that has, itself, been used extensively in radio oceanography applications; and 2) the bistatic electromagnetic coupling coefficient is shown to reduce exactly to the monostatic result when backscattering geometry is imposed. The model is also depicted and discussed based on simulated data.**

***Index Terms*—Bistatic cross section, Doppler spectrum, high-frequency (HF) ground-wave radar.**

I. Introduction

HIGH-FREQUENCY (HF) radar has been an important tool for remote sensing the sea state for three decades. Much of the pioneering activity as well as a preponderance of ensuing analysis and experimentation rests on the work of Barrick [1], [2]. Barrick's monostatic radar cross sections of the ocean surface incorporating a plane-wave source and based on Rice's perturbation method [3] have received wide acceptance in the radio-oceanographic community. Subsequently, Walsh *et al.* [4] produced monostatic results using a generalized function approach for the scattering of HF electromagnetic radiation [5], [6] from rough surfaces. In [4], a pulse dipole source is assumed and a finite scattering patch is incorporated. Validation of these models has likewise been extensive (see, for example, [7]–[10]). Hisaki and Tokuda [11], [12] have also presented an HF monostatic model to second order for scattering from a finite ocean patch via a perturbation technique. Additionally, theoretical work by Anderson *et al.* [13] has been validated by bistatic field experiments [14], [15].

Most recently, based on [6] and [16], Gill and Walsh [17] developed HF bistatic models for the first- and second-order ocean cross sections. Because of the lack of availability of bistatically received HF field data, the work in [17] relies on its similarity to earlier monostatic results as a form of validation. However, the approach taken, which gave rise to a more general result than previously presented, precluded the possibility of exact comparison of the bistatic and monostatic cases. In this paper, beginning with the expression for the vertically polarized electric field appearing in [6], a new approach is taken which produces a bistatic cross section to second order for a finite patch of ocean which is distant from the source and receiver—called here "patch scatter." For the case of backscatter, the new result is seen to reduce exactly to the extensively validated monostatic model appearing in [4]. Furthermore, while there are several components to the scattering cross section, it is the portion being calculated here that is of the most significance for inversion processes used in ocean surface interrogation (see [18]). The procedure for calculating all orders of scatter, which formally gives results to third-order, is given in [4] and [6]. In general, the first- and second-order spectrum dominates over the third- and higher orders.

In Section II, the second-order scattering field equation is presented as an asymptotic two-dimensional (2-D) double-convolution form [6]. The equation is expanded in integral form first to give the second-order field for scattering from a rough time-invariant surface for a dipole source. By specifying a surface to be time-varying and representable by a Fourier series whose coefficients are random variables, the field for double scattering on a patch of ocean is presented. Earlier results from the first-order models [17] are combined with the new analysis to give the total patch scatter cross section to second order in scatter. Section III outlines how the new bistatic result reduces exactly to that of the monostatic case when the bistatic angle is chosen to be zero—i.e., the condition for backscatter. This involves first a comparison of the general cross-section forms and second the reduction of the second-order electromagnetic coupling coefficient to that for backscatter. Section IV depicts the derived cross sections for a variety of radar and ocean surface parameters. A brief summary and the direction of ongoing relevant work are addressed in Section V.

Manuscript received November 16, 2004; accepted October 21, 2005. This work was supported by Natural Sciences and Engineering Research Council of Canada Grants to Dr. E. Gill NSERC 238263-01 and NSERC 200435 and Dr. J. Walsh NSERC 203478. **Associate Editor: L. R. Wyatt**.

The authors are with the Faculty of Engineering and Applied Science, Memorial University of Newfoundland, St. John's, NL A1B 3X5, Canada (e-mail: egill@engr.mun.ca; weimin@engr.mun.ca).

Digital Object Identifier 10.1109/JOE.2006.886228

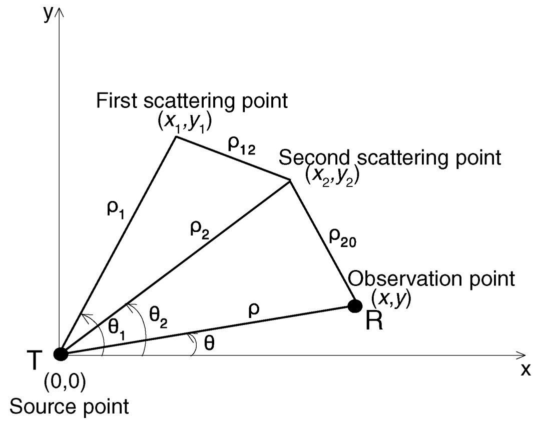

Fig. 1. Second-order bistatic scatter geometry.

II. Second-Order Radar Cross Section for Patch Scatter

A. Second-Order Field for a Time-Invariant Surface

The small height, small slope analysis carried out by Walsh and Gill [6] for the scattering of vertical polarized HF radiation from a good-conducting rough surface gives the general form of the second-order field (see [6, eq. (54)]) as

$$(E_{0n}^{+})_2 \approx -jkC_0\Bigg\{\nabla_{xy}(\xi) \cdot \nabla_{xy}\left[\hat{\rho}\cdot\nabla_{xy}(\xi)F(\rho)\frac{e^{-jk\rho}}{2\pi\rho}\overset{xy}{*}F(\rho)\frac{e^{-jk\rho}}{2\pi\rho}\right] \overset{xy}{*}F(\rho)\frac{e^{-jk\rho}}{2\pi\rho}\Bigg\}. \quad (1)$$

This is the starting point of the current analysis. Here, ∇_{xy} is the planar gradient operator while $\overset{xy}{*}$ represents a 2-D spatial convolution. The surface ξ is a function of spatial variables x and y or, equivalently, ρ and θ in polar coordinates. The $F()$ is the usual Sommerfeld attenuation function, k is the wave number of the radar transmitted signal, C_0 is a source-dependent constant in the temporal Fourier transform domain, and since in this work, a dipole source of length $\Delta\ell$ and carrying a current I is being considered, its expression is well-known to be $I\Delta\ell k^2/j\omega\epsilon_0$ where ω and ϵ_0 are radian frequency of the radiation and the permittivity of free space, respectively. As shown in Fig. 1, the radiation from the radar transmitter position $T(0,0)$ scatters in all directions from a general point (x_1,y_1). Some of the energy scatters again at point (x_2,y_2), and a portion of this is received at $R(x,y)$. The field scattering from (x_1,y_1) and reaching (x_2,y_2) is represented by the inner convolution of (1). The dot product of the gradient (∇_{xy}) of this convolution with the surface gradient $(\nabla_{xy}(\xi))$ represents the scatter from (x_2,y_2). The final convolution gives the received field at $R(x,y)$. Therefore, as noted in [6], (1) includes two scatters from any and all points on the surface.

Equation (1) is an asymptotic 2-D spatial-convolution expression, which is valid for the received field when the scattering occurs a great distance from the source—i.e., when ρ_1 is large. Gill and Walsh [17] used this equation to develop the second-order bistatic HF radar cross section for patch scatter. However, as already noted, because their total analysis was intended to reveal other components of the scatter, their result could not be shown to reduce exactly to earlier monostatic models. This can be attributed to the order of carrying out the inner convolution and its gradient appearing in (1). In [17], the identity

$$\nabla_{xy}(A\overset{xy}{*}B) = A\overset{xy}{*}\nabla_{xy}(B) = B\overset{xy}{*}\nabla_{xy}(A) \quad (2)$$

was used and the inner convolution in (1) was performed after application of the gradient. While the form of the result was comparable to the monostatic models, the approximations involved did not produce the usual form of the backscatter electromagnetic coupling coefficient. Here, the general result in (1) is again implemented to produce a bistatic patch scatter cross section at HF, but this time the result is established by carrying out the inner convolution before its gradient.

Using analysis involving a 2-D stationary phase approach [19] similar to that in [6], the field equation for patch scatter becomes (3), as shown at the bottom of the page, where P_{mn} is the Fourier coefficient of a surface component whose wave vector is $\vec{K}_{mn} = Nm\hat{x} + Nn\hat{y}$, $\vec{K}_{pq}$ is the wave vector of the second surface component, and $\vec{K}_{rs}$ is the sum $(\vec{K}_{mn} + \vec{K}_{pq})$ of the scatter wave vectors whose direction is θ_{rs}. The fundamental surface wave number appears as N.

Equation (3) may now be treated using a one-dimensional (1-D) stationary phase procedure. The stationary phase integration is accomplished via an elliptic coordinate (μ,δ) transformation similar to that described in [16]. That is (with reference to Fig. 1), the following is true:

1) rotation of the axes by θ, i.e.,

$$x_2 = x_2'\cos\theta - y_2'\sin\theta$$
$$y_2 = x_2'\sin\theta + y_2'\cos\theta; \quad (4)$$

2) shift of the origin in the (x_2', y_2') plane to a position halfway along ρ

$$x_2'' = x_2' - \frac{\rho}{2}$$
$$y_2'' = y_2' \quad (5)$$

$$(E_{0n}^{+})_2 \approx \frac{-kC_0}{(2\pi)^2}\sum_{mn}\sum_{pq}P_{mn}P_{pq}\int_{x_2}\int_{y_2}F(\rho_2)F(\rho_{20})\,\frac{(\vec{K}_{mn}\cdot\hat{\rho}_2)[\vec{K}_{pq}\cdot(\vec{K}_{mn}-k\hat{\rho}_2)]}{\sqrt{\vec{K}_{mn}\cdot(\vec{K}_{mn}-2k\hat{\rho}_2)}}\,\frac{e^{j\rho_2[K_{rs}\cos(\theta_{rs}-\theta_2)-k]-jk\rho_{20}}}{\rho_2\rho_{20}}dx_2dy_2 \quad (3)$$

then

$$x_2 = \left(x_2'' + \frac{\rho}{2}\right)\cos\theta - y_2''\sin\theta$$
$$y_2 = \left(x_2'' + \frac{\rho}{2}\right)\sin\theta + y_2''\cos\theta; \tag{6}$$

3) conversion to elliptic coordinates

$$x_2'' = \frac{\rho}{2}\cosh\mu\cos\delta$$
$$y_2'' = \frac{\rho}{2}\sinh\mu\sin\delta. \tag{7}$$

This results in

$$x_2 = \frac{\rho}{2}[(1+\cosh\mu\cos\delta)\cos\theta - \sinh\mu\sin\delta\sin\theta]$$
$$y_2 = \frac{\rho}{2}[(1+\cosh\mu\cos\delta)\sin\theta + \sinh\mu\sin\delta\cos\theta]. \tag{8}$$

This gives

$$\rho_2 = \frac{\rho}{2}(\cosh\mu + \cos\delta)$$
$$\rho_{20} = \frac{\rho}{2}(\cosh\mu - \cos\delta) \tag{9}$$

$$\theta_2 = \tan^{-1}\left(\frac{y_2}{x_2}\right) = \tan^{-1}\left[\frac{(1+\cosh\mu\cos\delta)\sin\theta + \sinh\mu\sin\delta\cos\theta}{(1+\cosh\mu\cos\delta)\cos\theta - \sinh\mu\sin\delta\sin\theta}\right]. \tag{10}$$

By using the above transformation, (3) becomes (11), as shown at the bottom of the page, whence we write for the δ integral (12), as shown at the bottom of the page.

For bistatic operation, where ρ will be on the order of tens of kilometers, $(\rho K_{rs}/2)$ will be a large parameter for quite an acceptable range of surface wave numbers K_{rs}. Furthermore, the Sommerfeld attenuation functions are slowly varying, especially for the ocean surface at HF. Thus, a stationary phase integration may be used in (12) to yield (13), as shown at the bottom of the page. Additionally, a stationary phase condition on δ is given by

$$\tanh\delta = \tanh\mu\tan(\theta_{rs} - \theta). \tag{14}$$

Gill and Walsh [16], [17] have shown that at the patch scatter position the surface wave vector $\vec{K}_{rs}$ is along the normal ($\mathbf{N}$) to the scattering ellipse (see Fig. 2), and the angle between the transmitter and receiver as viewed from the scatter point is bisected by the ellipse normal at that point. Each portion of this

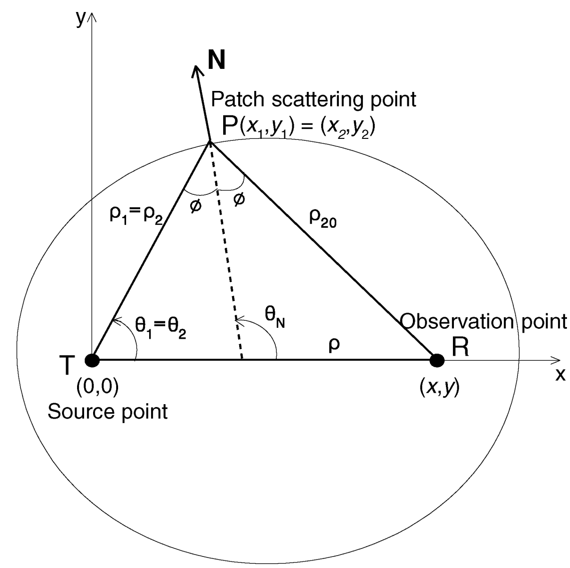

Fig. 2. Depiction of the geometry associated with the second-order stationary phase condition. R and T are receiver and transmitter, respectively.

$$(E_{0n}^{+})_2 \approx \frac{-kC_0}{(2\pi)^2}\sum_{mn}\sum_{pq} P_{mn}P_{pq}\, e^{j(\rho K_{rs}/2)\cos(\theta_{rs}-\theta)} \int_0^{\infty} e^{-j\rho k\cosh\mu} \cdot \left(\int_0^{2\pi} F(\rho_2)F(\rho_{20})\, \frac{(\vec{K}_{mn}\cdot\hat{\rho}_2)[\vec{K}_{pq}\cdot(\vec{K}_{mn}-k\hat{\rho}_2)]}{\sqrt{\vec{K}_{mn}\cdot(\vec{K}_{mn}-2k\hat{\rho}_2)}}\, e^{j(\rho K_{rs}/2)[\cosh\mu\cos\delta\cos(\theta_{rs}-\theta)+\sinh\mu\sin\delta\sin(\theta_{rs}-\theta)]} d\delta\right) d\mu \tag{11}$$

$$I_\delta = \int_0^{2\pi} \frac{(\vec{K}_{mn}\cdot\hat{\rho}_2)[\vec{K}_{pq}\cdot(\vec{K}_{mn}-k\hat{\rho}_2)]}{\sqrt{\vec{K}_{mn}\cdot(\vec{K}_{mn}-2k\hat{\rho}_2)}} F(\rho_2)F(\rho_{20})\, e^{j(\rho K_{rs}/2)[\cosh\mu\cos\delta\cos(\theta_{rs}-\theta)+\sinh\mu\sin\delta\sin(\theta_{rs}-\theta)]} d\delta \tag{12}$$

$$I_\delta \approx \sqrt{2\pi}\frac{(\vec{K}_{mn}\cdot\hat{\rho}_2)[\vec{K}_{pq}\cdot(\vec{K}_{mn}-k\hat{\rho}_2)]}{\sqrt{\vec{K}_{mn}\cdot(\vec{K}_{mn}-2k\hat{\rho}_2)}} F(\rho_2)F(\rho_{20})\, e^{j(\rho K_{rs}/2)[\cosh\mu\cos\delta\cos(\theta_{rs}-\theta)+\sinh\mu\sin\delta\sin(\theta_{rs}-\theta)]} \cdot \left(\frac{1}{j\frac{\rho K_{rs}}{2}[\cosh\mu\cos\delta\cos(\theta_{rs}-\theta)+\sinh\mu\sin\delta\sin(\theta_{rs}-\theta)]}\right)^{1/2} \tag{13}$$

bisection is seen in Fig. 2 as angle ϕ. Based on these results, (13) becomes

$$I_\delta \approx \sqrt{2\pi}\frac{(\vec{K}_{mn}\cdot\hat{\rho}_2)[\vec{K}_{pq}\cdot(\vec{K}_{mn}-k\hat{\rho}_2)]}{\sqrt{\vec{K}_{mn}\cdot(\vec{K}_{mn}-2k\hat{\rho}_2)}}\left(\frac{1}{\pm\sqrt{\cos\phi}}\right) \cdot\frac{F(\rho_2)F(\rho_{20})}{\sqrt{K_{rs}\rho_{s21}}}e^{\pm j\rho_{s21}K_{rs}\cos\phi}e^{\mp\pi/4} \quad (15)$$

where

$$\rho_{s21}=\frac{\rho_2+\rho_{20}}{2}=\frac{\rho}{2}\cosh\mu. \quad (16)$$

On inserting (15) and (16) and rewriting the μ integral in terms of ρ_{s21}, (11) becomes (17), as shown at the bottom of the page. Equation (17) is the result when the source is a continuously excited dipole. Employing a pulsed dipole source in this equation, after the manner explained in detail in [17], results in a time-dependent E-field of the form

$$\begin{aligned}(E_{0n}^{+})_2(t) \approx{}& \frac{-j\eta_0\Delta\ell I_0k_0^2}{(2\pi)^{3/2}}\sum_{mn}\sum_{pq}P_{mn}P_{pq}\\ &\cdot e^{j\vec{\rho}/2\cdot\vec{K}_{rs}}e^{jk_0\Delta\rho_{s21}}e^{-j\pi/4}\\ &\cdot\Gamma_{EP}\sqrt{K_{rs}\cos\phi_0}\frac{F(\rho_{02},\omega_0)F(\rho_{020},\omega_0)}{\sqrt{\rho_{s021}[\rho_{s021}^2-(\frac{\rho}{2})^2]}}\\ &\cdot e^{j\rho_{s021}K_{rs}\cos\phi_0}\Delta\rho_{s21}\\ &\cdot Sa\left[\frac{\Delta\rho_{s21}}{2}\left(\frac{K_{rs}}{\cos\phi_0}-2k_0\right)\right]. \end{aligned} \quad (18)$$

Here, $Sa(x)=\sin x/x$, I_0 is the peak current on a pulsed dipole of length $\Delta\ell$, $\Delta\rho_{s21}$ is the patch width, and ϕ_0 and k_0 are representative values of the bistatic angle and the radiation wave number, respectively. The factor Γ_{EP}, commonly referred to as an electromagnetic coupling coefficient, has the form

$$\Gamma_{EP}=\frac{-(\vec{K}_{mn}\cdot\hat{\rho}_2)[\vec{K}_{pq}\cdot(\vec{K}_{mn}-k_0\hat{\rho}_2)]}{K_{rs}\cos\phi_0\sqrt{\vec{K}_{mn}\cdot(\vec{K}_{mn}-2k_0\hat{\rho}_2)}}. \quad (19)$$

This is the factor which distinguishes (18) from a similar expression derived in [17, eq. (7)]. As already intimated and as is discussed in Section III, this form of the bistatic electric field equation allows for direct comparison between bistatic cross sections obtained in Section II-B and the earlier monostatic results derived from this theory.

B. *Second-Order Bistatic Cross Section of the Ocean Surface*

The process of determining the actual bistatic radar cross section from the electric field expression is well understood and presented in detail in, for example, [17]. It essentially involves the following steps: 1) introducing the ocean surface into (18) by allowing the Ps to become time-varying, zero-mean Gaussian random variables; 2) finding the autocorrelation of the total electric field expression (all relevant orders of scatter); 3) Fourier transforming the result to obtain the power spectral density; and 4) using the result from step 3) in the radar range equation to write down the cross section. Carrying out these details with respect to (18) leads to the second-order HF bistatic "patch scatter" cross section as given by (20), shown at the bottom of the page, where $S(\cdot)$ is the ocean spectrum, $\vec{K}_1$ and $\vec{K}_2$ are ocean wave vectors of magnitude K_1, K_2 and direction $\theta_{\vec{K}_1}$, $\theta_{\vec{K}_2}$, respectively, ω_d is the Doppler frequency, and $\delta(\cdot)$ is the delta function constraint. The factor Γ_P is a symmetricized coupling coefficient consisting of the sum of an electromagnetic term Γ_{EP} and a hydrodynamic term Γ_H given by

$$\Gamma_H=\frac{1}{2}\left\{K_1+K_2+\frac{g}{w_1w_2}(K_1K_2-\vec{K}_1\cdot\vec{K}_2)\cdot\left[\frac{gK+(w_1+w_2)^2}{gK-(w_1+w_2)^2}\right]\right\}$$

where ω_1 and ω_2 are angular frequencies of the ocean waves responsible for the scattering. Γ_H arises from a single electromagnetic scatter from second-order ocean waves. This feature has been extensively addressed by several investigators (e.g., [2] and [17]). Last, it should be noted that $\vec{K}_1$ and $\vec{K}_2$ are the same as $\vec{K}_{mn}$ and $\vec{K}_{pq}$, respectively, and are wave vectors of the scatterers on the patch.

$$\begin{aligned}(E_{0n}^{+})_2 \approx{}& \frac{-kC_0}{(2\pi)^{3/2}}\sum_{mn}\sum_{pq}P_{mn}P_{pq}\,e^{j\vec{\rho}/2\cdot\vec{K}_{rs}}\\ &\cdot\int_{\rho/2}^{\infty}e^{-j2\rho_{s21}k}\frac{(\vec{K}_{mn}\cdot\hat{\rho}_2)[\vec{K}_{pq}\cdot(\vec{K}_{mn}-k\hat{\rho}_2)]}{\sqrt{\vec{K}_{mn}\cdot(\vec{K}_{mn}-2k\hat{\rho}_2)}}\frac{1}{\pm\sqrt{K_{rs}\cos\phi}}\frac{F(\rho_2)F(\rho_{20})}{\sqrt{\rho_{s21}[\rho_{s21}^2-(\frac{\rho}{2})^2]}}e^{\pm j\rho_{s21}K_{rs}\cos\phi}e^{\mp\pi/4}d\rho_{s21}\end{aligned} \quad (17)$$

$$\begin{aligned}\sigma_{2EP}(\omega_d)={}&2^3\pi k_0^2\Delta\rho_{s21}\sum_{m_1=\pm1}\sum_{m_2=\pm1}\int_{-\infty}^{\infty}\int_{-\pi}^{\pi}\int_{-\infty}^{\infty}S(m_1\vec{K}_1)S(m_2\vec{K}_2)\\ &\cdot|\Gamma_P|^2K_{rs}^2\cos\phi_0\,Sa^2\left[\frac{\Delta\rho_{s21}}{2}\left(\frac{K_{rs}}{\cos\phi_0}-2k_0\right)\right]\delta(\omega_d+m_1\sqrt{gK_1}+m_2\sqrt{gK_2})\,K_1dK_1d\theta_{\vec{K}_1}dK_{rs}\end{aligned} \quad (20)$$

III. Analytical Verification of Cross Section

A. Comparison With Monostatic Forms

It is readily checked that (20) has the same form as the result derived by Gill [17] but with a different electromagnetic coupling coefficient, this difference arising from the order of analysis taken in (1) as discussed in Section II. We now proceed to show that (20) reduces to the general form of the monostatic results given by Barrick's perturbation method [2] and the generalized function approach taken by Walsh *et al.* [4]. To facilitate this and in keeping with those works, we seek a result for a large scattering patch. In particular, using the relationship

$$\lim_{M\to\infty} Sa^2(Mx) = \pi\delta(x) \tag{21}$$

in (20), where it is assumed $\Delta\rho_{s21} \to \infty$, allows us to write

$$\begin{aligned}\Delta\rho_{s21} Sa^2 &\left[\frac{\Delta\rho_{s21}}{2}\left(\frac{K_{rs}}{\cos\phi_0} - 2k_0\right)\right] \\ &= 2\cos\phi_0 \frac{\Delta\rho_{s21}}{2\cos\phi_0} Sa^2\left[\frac{\Delta\rho_{s21}}{2\cos\phi_0}\left(K_{rs} - 2k_0\cos\phi_0\right)\right] \\ &= 2\pi\cos\phi_0 \delta\left(K_{rs} - 2k_0\cos\phi_0\right).\end{aligned} \tag{22}$$

Inserting this expression into (20) and using the Dirac delta function to evaluate the K_{rs} integral result in (23), as shown at the bottom of the page. For monstatic operation, $\phi_0 = 0$ and (23) simplifies to (24), as shown at the bottom of the page. While the notation and normalizations used by Barrick [2] differ from this work, the final results are identical in form. Furthermore, (24) is exactly the same—in detail as well as in form—as that given in [4]. To prove this, the electromagnetic coupling coefficient must be further examined.

B. Electromagnetic Coupling Coefficient

While the deep-water hydrodynamic coupling coefficient appears in all similar analyses (see, for example, [20]), the electromagnetic term differs. In particular, here we wish to establish that while the expression given in (19), with the new symbols introduced for the scattering wave vectors, is

$$\Gamma_{EP} = \frac{-(\vec{K}_1\cdot\hat{\rho}_2)[\vec{K}_2\cdot(\vec{K}_1 - k_0\hat{\rho}_2)]}{K_{rs}\cos\phi_0\sqrt{\vec{K}_1\cdot(\vec{K}_1 - 2k_0\hat{\rho}_2)}} \tag{25}$$

it can be shown to reduce in a symmetricized fashion to the monostatic coupling coefficient

$${}_s\Gamma_{EP} = \frac{-j\left|\vec{K}_1\times\vec{K}_2\right|^2}{2K^2\sqrt{\vec{K}_1\cdot\vec{K}_2}} \tag{26}$$

given by Walsh *et al.* [4]. It should be noted that in (25) $K_{rs} = 2k_0\cos\phi_0$ as dictated by the delta function in (22). For monostatic operation $\phi_0 = 0$ and since K in (26) has a value of $2k_0$, it is obvious that, for this case, $K_{rs}\cos\phi_0$ and K are identical. Furthermore, it is clear that ${}_s\Gamma_{EP}$ is either positive real or imaginary (and never complex). Thus, when it is added to Γ_H, which is itself positive real, the magnitude of the sum will be greater than or equal to either of the individual contributions. While this is true, it is the hydrodynamic portion which is most significant in ocean parameter applications (see [18]).

It is easy to show from the patch-scattering geometry (see Fig. 2) that

$$\hat{\rho}_2 = \hat{x}\cos\theta_2 + \hat{y}\sin\theta_2 \tag{27}$$

can be written as

$$\hat{\rho}_2 = \hat{N}\cos\phi_0 + \hat{\theta}_N\sin\phi_0 \tag{28}$$

where the unit normal $\hat{N}$ and its orthogonal angular counterpart $\hat{\theta}_N$ may be written as

$$\begin{aligned}\hat{N} &= \hat{x}\cos(\theta_2+\phi_0) + \hat{y}\sin(\theta_2+\phi_0)\\ \hat{\theta}_N &= -\hat{x}\sin(\theta_2+\phi_0) + \hat{y}\cos(\theta_2+\phi_0).\end{aligned} \tag{29}$$

For backscattering ($\phi_0 = 0$) and

$$\hat{\rho}_2 = \hat{N}. \tag{30}$$

In Section II, it was established that $\vec{K}_{rs}$ is along the $\hat{N}$ direction so that (on dropping the rs subscripts to conform to the notation in Walsh *et al.* [4])

$$\vec{K} = 2k_0\cos\phi_0\hat{N} = 2k_0\hat{N} \tag{31}$$

and

$$\hat{\rho}_2 = \hat{N} = \frac{\vec{K}}{2k_0} = \hat{K}. \tag{32}$$

Furthermore

$$\vec{K}_1 + \vec{K}_2 = 2k_0\hat{K}. \tag{33}$$

$$\sigma_{2P}(\omega_d) = 2^6\pi^2k_0^4\sum_{m_1=\pm1}\sum_{m_2=\pm1}\int_{-\pi}^{\pi}\int_{-\infty}^{\infty} S(m_1\vec{K}_1)\,S(m_2\vec{K}_2)|\Gamma_P|^2\cos^4\phi_0\,\delta(\omega_d + m_1\sqrt{gK_1} + m_2\sqrt{gK_2})\,K_1dK_1d\theta_{\vec{K}_1}. \tag{23}$$

$$\sigma_{2P}(\omega_d) = 2^6\pi^2k_0^4\sum_{m_1=\pm1}\sum_{m_2=\pm1}\int_{-\pi}^{\pi}\int_{-\infty}^{\infty} S(m_1\vec{K}_1)\,S(m_2\vec{K}_2)|\Gamma_P|^2\,\delta(\omega_d + m_1\sqrt{gK_1} + m_2\sqrt{gK_2})\,K_1dK_1d\theta_{\vec{K}_1}. \tag{24}$$

Substituting (32), (33), and $\phi_0 = 0°$ into (25)

$$\begin{aligned}\Gamma_{EP} &= \frac{-(\vec{K}_1 \cdot \hat{K})[\vec{K}_2 \cdot (\vec{K}_1 - k_0\hat{K})]}{K\sqrt{\vec{K}_1 \cdot (\vec{K}_1 - 2k_0\hat{K})}} \\ &= \frac{-(\vec{K}_1 \cdot \vec{K})[\vec{K}_2 \cdot (2\vec{K}_1 - 2k_0\hat{K})]}{2K^2\sqrt{\vec{K}_1 \cdot (-\vec{K}_2)}} \\ &= \frac{-[\vec{K}_1 \cdot (\vec{K}_1 + \vec{K}_2)][\vec{K}_2 \cdot (\vec{K}_1 - \vec{K}_2)]}{j2K^2\sqrt{\vec{K}_1 \cdot \vec{K}_2}} \\ &= \frac{j[{K_1}^2 + K_1K_2\cos(\theta_{\vec{K}_1} - \theta_{\vec{K}_2})]}{2K^2\sqrt{\vec{K}_1 \cdot \vec{K}_2}} \\ &\quad \cdot [K_1K_2\cos(\theta_{\vec{K}_1} - \theta_{\vec{K}_2}) - {K_2}^2] \\ &= \frac{-j\left|\vec{K}_1 \times \vec{K}_2\right|^2}{2K^2\sqrt{\vec{K}_1 \cdot \vec{K}_2}} + \frac{j\vec{K}_1 \cdot \vec{K}_2({K_1}^2 - {K_2}^2)}{2K^2\sqrt{\vec{K}_1 \cdot \vec{K}_2}}. \quad (34)\end{aligned}$$

Implementation of the cross section in (24) involves a summation over all wave numbers and as a result a "symmetricized" form of the coupling coefficient may be written as

$${}_s\Gamma_{EP}(\vec{K}_1, \vec{K}_2) = \frac{\Gamma_{EP}(\vec{K}_1, \vec{K}_2) + \Gamma_{EP}(\vec{K}_2, \vec{K}_1)}{2}. \quad (35)$$

Applying this to (34) allows us to write

$${}_s\Gamma_{EP} = \frac{-j\left|\vec{K}_1 \times \vec{K}_2\right|^2}{2K^2\sqrt{\vec{K}_1 \cdot \vec{K}_2}} \quad (36)$$

which is clearly identical to (26). Therefore, the bistatic radar cross section of (20) properly reduces in all respects to the existing monostatic models. These models have been extensively validated during experiments carried out on the Canadian east coast [7]–[10].

IV. Depiction and Discussion of the Cross-Section Models

The computation of the models developed in Section II is aided by adapting monostatic techniques presented by Lipa and Barrick [20] to the bistatic case as is discussed by Gill and Walsh [17]. The radar cross section, normalized to patch area, is calculated, as is commonly done, using a Pierson–Moskowiz model [21] with a cardiod directional distribution for the directional ocean waveheight spectrum of a wind-driven sea. For computations of the bistatic cross section, wind speed and direction, radar frequency, patch width and location, and bistatic angle are input to the model. The effects of bistatic angle, wind speed and direction, and operating frequency are examined. Finally, because of its relevancy to the overall discussion of the cross-section plots, the first-order bistatic cross section derived in [17] and [22] is given as

$$\sigma_1(\omega_d) = 2^4\pi k_0^2\Delta\rho_s \sum_{m=\pm1} S(m\vec{K})\frac{K^{5/2}\cos\phi_0}{\sqrt{g}} \cdot Sa^2\left[\frac{\Delta\rho_s}{2}\left(\frac{K}{\cos\phi_0} - 2k_0\right)\right] \quad (37)$$

where patch width has been labeled as $\Delta\rho_s$ and $\omega_d = -m\sqrt{gK}$. An example of how the scattering patch width affects this first-order result appears in Fig. 3 where the oscillatory features of the $Sa^2(\,)$ function have been smoothed using a Hamming window. The spectral smearing that is evident as the patch width diminishes would translate into a similar effect at each second-order Doppler point had the $Sa^2(\,)$ function been retained in calculating $\sigma_{2P}(\omega_d)$.

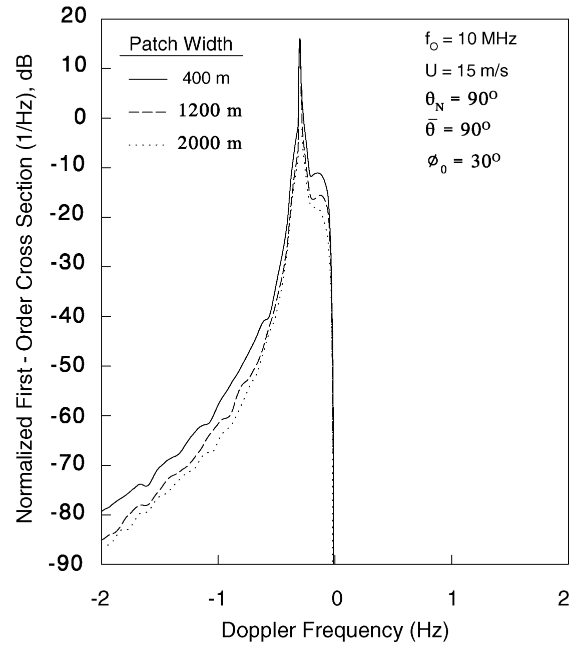

Fig. 3. Effect of radial patch width on the first-order cross section. The wind is outward along the ellipse normal at the scattering patch resulting in nonzero results for the negative Doppler region only.

Fig. 4 shows the effect of increasing bistatic angle for an operating frequency of 25 MHz, wind speed of 15 m/s, wind direction of 180°, an ellipse normal angle of 90°, and patch width of 2 km. The wind direction is referenced to the x-axis. Peaks B^- and B^+ are first-order maxima positions (Bragg peaks) which from (37) may be seen to occur when the Doppler frequency is $(\pm\sqrt{2k_0 g\cos\phi_0})/(2\pi)$ Hz. As the bistatic angle increases, both of these Bragg frequencies (f_B) move closer to zero Doppler. The singularities labeled P_1^- and P_1^+ are the $\pm\sqrt{2}f_B$ positions resulting from second-order hydrodynamic effects as extensively discussed by Lipa and Barrick [20] in the monostatic context and Gill and Walsh [17] for earlier bistatic analyses. The P_2s and P_3s are corner reflector peaks which can be shown, as in [17], to appear at Doppler frequencies (f_d) given by

$$f_d = \pm 2^{3/4}\sqrt{\frac{(1 \pm \sin\phi_0)^{1/2}}{\cos\phi_0}}f_B. \quad (38)$$

For the monostatic case [Fig. 4(a)], P_2s and P_3s obviously reduce to single positions in the regions $f_d > |f_B|$. Also, as the bistatic angle increases, the second-order patch scatter effects are greatly diminished and when $\phi_0 = 75°$, the highest contribution to the corner reflector phenomenon is masked by the $\sqrt{2}f_B$ singularity. In the latter case, the second contribution to the corner reflector is far removed from any region of interest in the Doppler spectrum.

Fig. 5 shows the relationship between the Doppler spectrum for a bistatic angle of 30° with that for monostatic operation

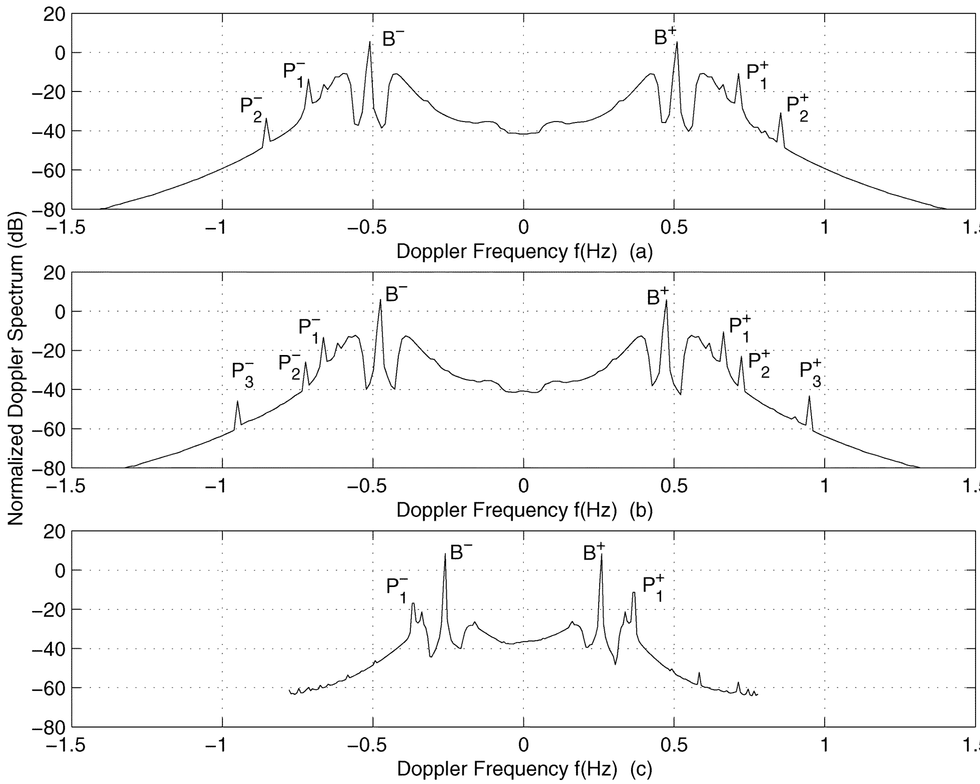

Fig. 4. Bistatic patch scatter Doppler spectra for different bistatic angles with wind direction of 0° and wind speed of 15 m/s. The bistatic angle is (a) 0°, (b) 30°, and (c) 75°.

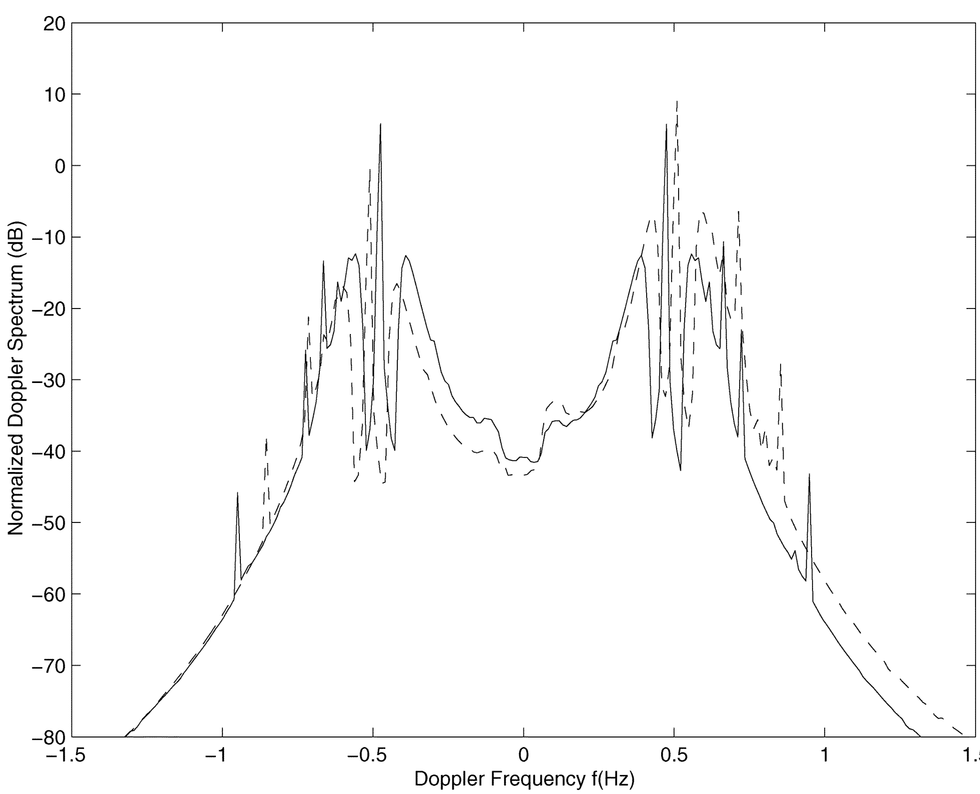

Fig. 5. Comparison of bistatic (solid line) patch scatter Doppler spectra with monostatic (dashed line) result.

when the wind direction referenced to the x-axis is 180° (or 90° to the ellipse normal which has figured significantly in this analysis), the operating frequency is 25 MHz and the wind speed is 15 m/s. For a complete monostatic system located at the transmitter site of the bistatic radar, the look direction for the stated scenario is 60° and the wind makes an angle of 120° with the

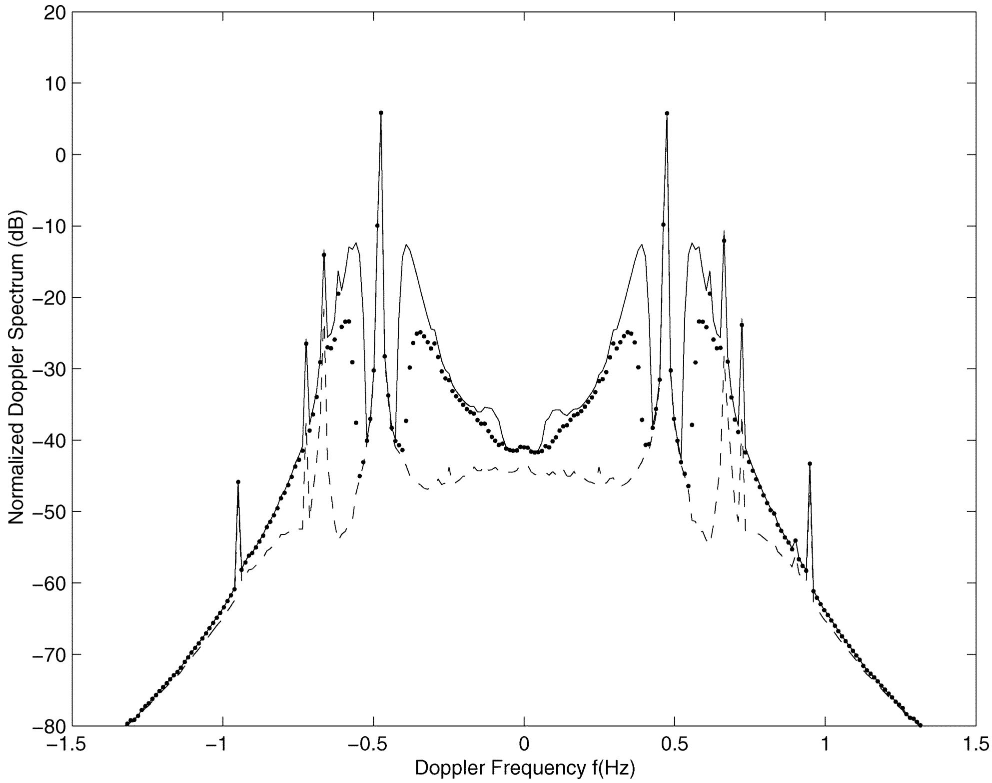

Fig. 6. Bistatic patch scatter Doppler spectra under different wind speeds with wind direction of 180°. Wind speed is 15 m/s (solid line), 10 m/s (dotted line), and 5 m/s (dashed line).

assumed narrow radar beam, with a component being inward along the beam. It may be seen from the figure that simultaneous bistatic and monostatic interrogation of the same patch of ocean provides a basis for extracting unambiguous directional information from the radar signal. This may be deduced by considering the fact that had wind been 0° to the x-axis, the bistatic spectrum would be unaffected but the relative powers in the monostatic Bragg peaks would shift (i.e., in the latter case, the left peak would be higher than the right) as a result of the wind having a component outward along the beam.

With respect to Fig. 5, it is also worthwhile to consider the seemingly unnatural behavior of the spectrum near-zero Doppler. The second-order integration in the near-zero Doppler region was carried out using a variable-step Simpson's rule. Repeatability of the results was checked by comparing the output for a range of integration steps. There are several reasons why the near-zero Doppler values here do not precisely match field data in this region. 1) This paper presents only the patch scatter portion of the second-order cross section. As noted in [17], there are other contributions to the total cross section (due to scattering near the antennas) which especially affect the near-zero Doppler region and increase the overall spectral value above that caused by patch-scatter alone. 2) There are often land echoes in real data. Clearly, these will contribute increased energy at zero Doppler. 3) There is often evidence that the transmit signal leaks into the receiver and while this signal is greatly diminished compared to the full signal it is strong enough to appear in the already relatively low scatter signal in the region being considered. It is thus not surprising that in the near-zero Doppler portion of the spectrum, there is an apparent discrepancy between simulations and field data.

From (20) and (37), it is clear that the radar cross sections are functions of the wave spectrum and hence of wind speed. Fig. 6 shows cross-section results for a variety of wind speeds, an operating frequency of 25 MHz, a wind direction of 180°, and a bistatic angle of 30°. It might be noted that the magnitudes of second-order bistatic Doppler spectra adjacent to the Bragg peaks are very sensitive to the change of wind speed. This reflects the fact that long ocean waves whose radar signatures are found in this Doppler region will carry a significant amount of spectral energy at higher wind speeds. Thus, as for the monostatic case, the second-order Doppler spectral values in this near-Bragg portion are very important in the process of inverting the cross sections to extract ocean surface state parameters such as the nondirectional wave spectrum, waveheight, and wind speed (see, for example, [8], [23], and [24]). The high-Doppler tails do not change significantly with wind speed. This is because the ocean waves responsible for the scattering associated with this portion of the Doppler spectrum lie in the saturated region of the ocean wave spectrum where the spectral energy is almost independent of wind speed. Also, as long as the Bragg wave stays within the saturated region of the ocean spectrum (this will depend on the length of the Bragg wave and, hence, on the operating frequency), the size of the first-order peaks is not significantly affected by wind speed.

Fig. 7 gives the bistatic cross sections under different wind directions with a constant wind speed of 15 m/s. Other parameters are the same as those in Fig. 6. At HF, the Bragg waves are gen-

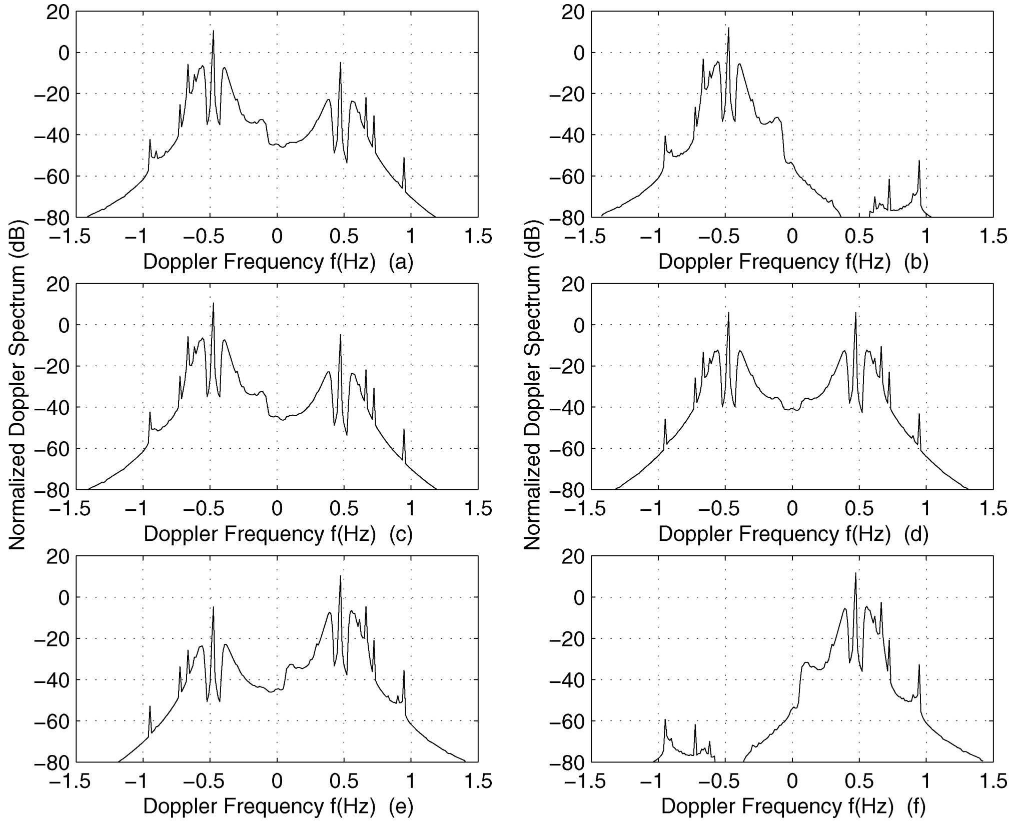

Fig. 7. Bistatic patch scatter Doppler spectra under different wind directions with wind speed of 15 m/s. The wind direction is (a) 45°, (b) 90°, (c) 135°, (d) 180°, (e) 225°, and (f) 270°.

erally short enough to respond quickly to changes in the local wind conditions. It is well known that the ratio of the intensities of the positive and negative peaks is highly sensitive to the wind direction. Taking a monostatic radar system for example, if the wind is perpendicular to the radar beam direction for a significant period of time, the Bragg peaks will carry similar amounts of energy. In the other extreme, the negative/positive Bragg peak will be enhanced when the wind direction is parallel/antiparallel to the radar beam direction. The same is true for bistatic operation provided the reference is taken with respect to the scattering ellipse normal rather than the radar beam direction. That is, the negative/positive Bragg peak will be enhanced when the wind direction has a component that is parallel/antiparallel to the ellipse normal direction. The antisymmetry that exists when wind direction φ_W changes to $\varphi_W + 180°$ is obvious from, for example, Fig. 7(b) and (f). The ratio of the approaching to receding Bragg energy is indicative of the (ambiguous) wind direction as has been discussed by several investigators (see, for example, [25]–[29]).

While the analysis here is suitable for the entire HF band, it is seen from Fig. 8 that there is a significant reduction in the near-Bragg second-order energy as the frequency drops—other parameters are the same as those in Fig. 6. This is again a well-known phenomenon and it dictates which part of the band should be employed for particular purposes. For example, the upper HF band is ideally suited to ocean wave measurement because this depends on the near-Bragg Doppler regions, but the useful range is reduced (to several tens of kilometers) due to the larger attenuation at these frequencies. On the other hand, for current measurements, which depend on the Bragg frequencies, a lower operating frequency may be used to obtain useful data well beyond a 200-km range [30]. It is seen that the strength of the Bragg peaks does not change significantly when operating frequency varies for the operating parameters given in the figure. As noted previously, the Bragg waves generally lie in the saturated region of the ocean wave spectrum. Of course, as the bistatic angle becomes very large, the $\cos\phi_0$ factor in (37) along with the relationship

$$f_B = 0.102\sqrt{f_0 \cos\phi_0} \tag{39}$$

where f_0 is the radar operating frequency in megahertz, dictate that both the Bragg frequency and its energy become significantly diminished.

V. Summary

In this paper, the development of a new second-order cross section model for the bistatic operation of HF radar in an ocean environment is undertaken. It begins with the second-order electric field equation for scatter from a time-invariant rough surface derived by Walsh and Gill [6]. Unlike previous work [17], the analysis here allows for a direct comparison to be made between the final result and earlier monostatic models [4] when a value of 0° is used for the bistatic scattering angle. This comparison is carried out at two levels. First, the complete form of the

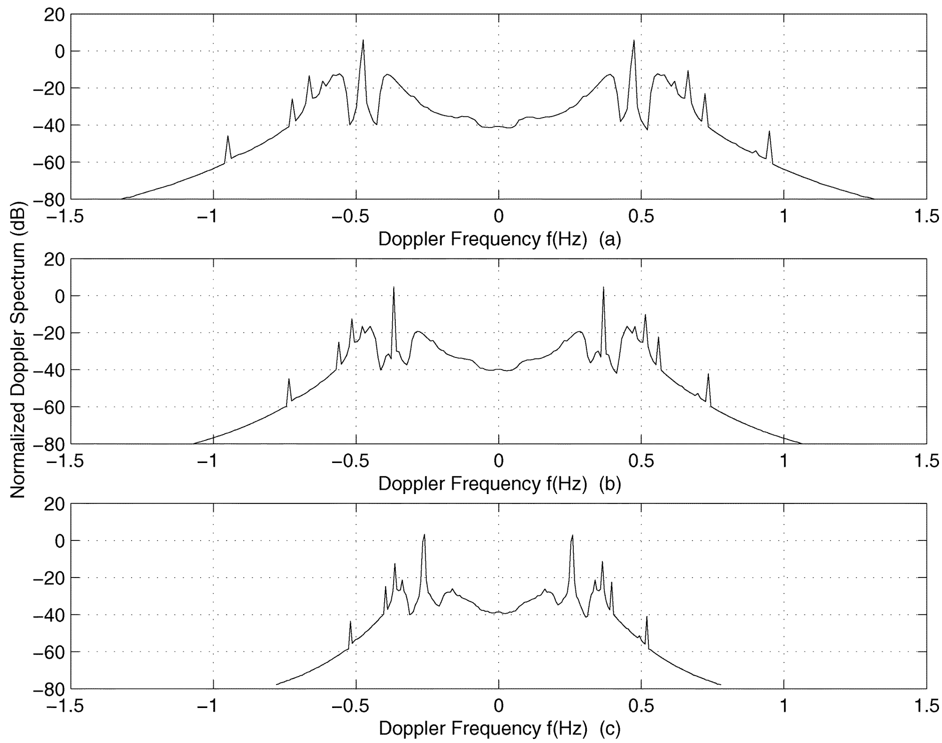

Fig. 8. Bistatic patch scatter Doppler spectra for different operating frequencies with wind direction of 0° and wind speed of 15 m/s. The radar frequency is (a) 25 MHz, (b) 15 MHz, and (c) 7.5 MHz.

bistatic HF radar cross section is shown to reduce to the general form of the monostatic models when appropriate geometry for backscatter is introduced. Second, the electromagnetic coupling coefficient for the bistatic case is seen to incorporate its monostatic counterpart.

The cross-section model is depicted and discussed based on a variety of simulated operating and environmental parameters. The utility of using a complete monostatic system in conjunction with a bistatic radar to eliminate the usual directional ambiguities is also briefly noted.

While measured sea-echo Doppler spectra invariably contain additive noise, such effects are not considered here. This is the subject of ongoing research and preliminary work has been presented by Gill and Walsh [31] in which white Gaussian noise is added to a time-domain model of the ocean clutter. Encouraging results on the recovery of ocean surface parameters by inverting noisy bistatic cross sections appear in [18] and [32]. With the ongoing expansion of the HF radar network on the Canadian east and west coasts, the recently developed models will be important in deducing environmental and surveillance information when these systems are operated in a bistatic mode.

REFERENCES

[1] D. E. Barrick, "First-order theory and analysis of MF/HF/VHF scatter from the sea," *IEEE Trans. Antennas Propag.*, vol. 20, no. 1, pp. 2–10, Jan. 1972.

[2] D. Barrick, "Remote sensing of sea state by radar," in *Remote Sensing of the Troposphere*, V. E. Derr, Ed.. Washington, DC: U.S. Government Printing Office, 1972, ch. 12, pp. 1–46.

[3] S. Rice, "Reflection of electromagnetic waves from a slightly rough surface," in *Theory of Electromagnetic Waves*, K. Kline, Ed.. New York: Wiley, 1951, pp. 351–378.

[4] J. Walsh, R. Howell, and B. Dawe, "Model development for evaluation studies of ground wave radar" Center Cold Ocean Resources Eng., Mem. Univ. Newfoundland, St. John's, NL, Canada, Contract Rep. 90-C14, 1990.

[5] J. Walsh and R. Donnelly, "A consolidated approach to two-body electromagnetic scattering problems," *Phys. Rev. A, Gen. Phys.*, vol. 36, pp. 4474–4485, 1987.

[6] J. Walsh and E. W. Gill, "An analysis of the scattering of high-frequency electromagnetic radiation from rough surfaces with application to pulse radar operating in backscatter mode," *Radio Sci.*, vol. 35, no. 6, pp. 1337–1359, 2000.

[7] E. Gill and J. Walsh, "Extraction of ocean wave parameters from HF backscatter received by a four-element array: Analysis and application," *IEEE J. Ocean. Eng.*, vol. 17, no. 4, pp. 376–386, Oct. 1992.

[8] R. Howell and J. Walsh, "Measurement of ocean wave spectra using narrow beam HF radar," *IEEE J. Ocean. Eng.*, vol. 18, no. 3, pp. 296–305, Jul. 1993.

[9] R. Howell and M. L. Khandekar, "Measuring ocean surface waves using HF ground wave radar–validation against a wave model," *Can. J. Remote Sens.*, vol. 19, no. 1, pp. 102–109, 1993.

[10] E. W. Gill, M. L. Khandekar, R. K. Howell, and J. Walsh, "Ocean surface wave measurement using a steerable high frequency narrow beam ground wave radar," *J. Atmos. Ocean. Technol.*, vol. 13, no. 3, pp. 703–713, 1996.

[11] Y. Hisaki and M. Tokuda, "VHF and HF sea echo Doppler spectrum for a finite illuminated area," *Radio Sci.*, vol. 36, no. 3, pp. 425–440, 2001.

[12] Y. Hisaki, "Doppler spectrum of radio wave scattering from ocean–like moving surfaces for a finite illuminated area," *Int. J. Remote Sens.*, vol. 24, no. 15, pp. 3075–3091, 2003.

[13] S. J. Anderson, J. Praschifka, and I. M. Fuks, "Multiple scattering of HF radiowaves propagating across the sea surface," *Waves in Radom Media*, vol. 8, pp. 283–302, 1998.

[14] ——, "Experimental investigations of multiple scattering of radio waves propagating across the sea surface," in *Proc. Int. Union Theoretical Appl. Mech. Symp. Mech. Electromagn. Waves Structured Media (IUTAM) 99/2*, Sydney, Australia, 1999.

[15] S. J. Anderson, "Directional wave spectrum measurement with multistatic HF surface wave radar," in *Proc IEEE Int. Geosci. Remote Sens. Symp. (IGARSS)*, 2000, pp. 2946–2949.

[16] E. W. Gill and J. Walsh, "Bistatic form of the electric field equations for the scattering of vertically polarized high-frequency ground wave radiation from slightly rough, good conducting surfaces," *Radio Sci.*, vol. 35, no. 6, pp. 1323–1335, 2000.
[17] ——, "High-frequency bistatic cross sections of the ocean surface," *Radio Sci.*, vol. 36, no. 6, pp. 1459–1475, 2001.
[18] J. Zhang and E. Gill, "Extraction of ocean wave spectra from simulated noisy bistatic high frequency radar data," *IEEE J. Ocean. Eng.*, vol. 31, no. 4, pp. 779–796, Oct. 2006.
[19] N. Beistein and R. Handelsman*, Asymptotic Expansion of Integrals*. Fort Worth, TX: Holt, Rinehart, and Winston, 1975.
[20] B. J. Lipa and D. E. Barrick, "Analysis methods for narrow-beam high-frequency radar sea echo" Nat. Ocean. Atmos. Admin., U.S. Dept. Commerce, Tech. Rep. ERL 420-WPL 56, 1982.
[21] W. Pierson and L. Moskowiz, "A proposed spectral form for fully developed seas based upon the similarity theory of S.A. Kitaigorodskii," *J. Geophys. Res.*, vol. 69, pp. 5181–5190, 1964.
[22] J. Walsh and B. Dawe, "Development of a model for the first order bistatic ocean clutter radar cross section for ground wave radars" Northern Radar Systems Limited, Contract Rep., 1994.
[23] D. E. Barrick, "Extraction of wave parameters from measured HF radar sea-echo Doppler spectra," *Radio Sci.*, vol. 12, no. 3, pp. 415–424, 1977.
[24] W. Huang, S. Wu, E. Gill, B. Wen, and J. Hou, "HF radar wind and wave measurement over the Eastern China Sea," *IEEE Trans. Geosci. Remote Sens.*, vol. 40, no. 9, pp. 1950–1955, Sep. 2002.
[25] A. E. Long and D. B. Trizna, "Mapping of North Atlantic winds by HF radar sea backscatter interpretation," *IEEE Trans. Antennas Propag.*, vol. 21, no. 5, pp. 680–685, Sep. 1973.
[26] M. L. Heron and R. J. Rose, "On the application of HF ocean radar to the observation of temporal and spatial changes in wind direction," *IEEE J. Ocean. Eng.*, vol. 11, no. 2, pp. 210–218, Apr. 1986.
[27] M. L. Heron and A. Prytz, "Wave height and wind direction from the HF coastal ocean surface radar," *Can. J. Remote Sens.*, vol. 28, no. 3, pp. 385–393, 2002.
[28] L. Wyatt, "An evaluation of wave parameters measured using a single HF radar system," *Can. J. Remote Sensing*, vol. 28, no. 2, pp. 205–218, 2002.
[29] W. Huang, E. Gill, S. Wu, B. Wen, Z. Yang, and J. Hou, "Measuring surface wind direction by monostatic HF ground-wave radar at the Eastern China Sea," *IEEE J. Ocean. Eng.*, vol. 29, no. 4, pp. 1032–1037, Oct. 2004.
[30] K. J. Hickey, E. Gill, J. A. Helbig, and J. Walsh, "Measurement of ocean surface currents using a long-range, high-frequency ground wave radar," *IEEE J. Ocean. Eng.*, vol. 19, no. 4, pp. 549–554, Oct. 1994.
[31] E. W. Gill and J. Walsh, "A relationship between external noise and the ocean clutter models for bistatic operation of pulsed high-frequency radar," in *Proc. IEEE Can. Conf. Electr. Comput. Eng.*, Toronto, ON, Canada, 2001, pp. 153–158.
[32] E. Gill, W. Huang, and J. Zhang, "An alternate analysis for the second-order high frequency bistatic radar cross section of the ocean surface – Patch scatter and its inversion," in *PROC. MTS/IEEE Conf. Exhibition OCEANS'2003*, 2003, pp. 2336–2340.

Eric Gill (M'00–SM'05) received the B.Sc. degree in physics in 1977 and the M.Eng. and Ph.D. degrees in electrical engineering in 1990 and 1999, respectively, all from Memorial University of Newfoundland, St. John's, NL, Canada.

In 1977, he was a Lecturer in Physics at the College of the North Atlantic (formerly, Cabot Institute of Applied Arts and Technology). Since 2000, he has been teaching and conducting research in theoretical and applied electromagnetics at the Faculty of Engineering and Applied Science, Memorial University. His special interest is in the scattering of high-frequency electromagnetic radiation from time-varying, randomly rough surfaces, with particular application to the use of ground-wave radar in remote sensing of the marine environment.

Dr. Gill is a member of the American Geophysical Union.

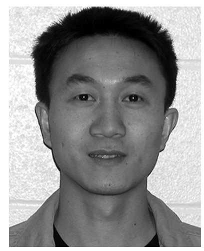

Weimin Huang received the B.S., M.S., and Ph.D. degrees in radio physics from Wuhan University, Wuhan, China, in 1995, 1997, and 2001, respectively.

Currently, he is a Postdoctoral Fellow in engineering electromagnetics at Memorial University of Newfoundland, St. John's, NL, Canada. His past and present research involves the mapping of oceanic-surface parameters via HF ground-wave radar.

John Walsh received the B.Eng. degree in electrical engineering from the Technical University of Nova Scotia, Halifax, NS, Canada, in 1968 and the Ph.D. degree from the University of Calgary, Calgary, AB, Canada, in 1971.

He worked as an Assistant Professor in the Electrical Engineering Department, Concordia University, Montreal, QC, Canada, from 1971 to 1972. In 1972, he joined the Faculty of Engineering and Applied Science at Memorial University of Newfoundland, St. John's, NL, Canada, where he is now a Professor Emeritus. He is also Vice-President of Research and Development for Northern Radar Systems Limited at St John's. His early research involved analysis of transmission lines and antenna systems. His major accomplishments include the development of analytical techniques for propagation and scatter from rough surfaces, mixed paths, and layered media, and the application of the results in ground-wave radar detection of ocean surface parameters and surface targets. He is author and coauthor of many refereed open-literature papers and major technical reports.